Geochemistry Geophysics Geosystems G3
AN ELECTRONIC JOURNAL OF THE EARTH SCIENCES
Published by AGU and the Geochemical Society

Article
Volume 4, Number 9
11 September 2003
9106, doi:10.1029/2003GC000542
ISSN: 1525-2027

Plume-transform interactions at ultra-slow spreading ridges: Implications for the Southwest Indian Ridge

Jennifer E. Georgen
MIT-WHOI Joint Program in Oceanography, Woods Hole Oceanographic Institution, Woods Hole, Massachusetts 02543, USA

Now at Graduate School of Oceanography, University of Rhode Island, 232 Horn Laboratory, South Ferry Road, Narragansett, Rhode Island 02882, USA (jgeorgen@gsosun1.gso.uri.edu)

Jian Lin
Department of Geology and Geophysics, Woods Hole Oceanographic Institution, Woods Hole, Massachusetts 02543, USA (jlin@whoi.edu)

[1] We explore a potentially important variable in controlling ridge-hot spot interaction, the effect of transform offsets in limiting along-axis flow of plume material. We focus on the Southwest Indian Ridge (SWIR), where the ‘‘transform damming’’ effect is likely to be pronounced because of both long offset lengths and large contrasts in lithospheric thickness across the transform faults due to the ultra-slow spreading rate. We investigate the degree to which transform faults affect axial asthenospheric flow by performing a series of three-dimensional (3-D) numerical experiments with simplified channel-flow geometry and extrapolating their results to the SWIR. 3-D mantle viscosity structure for a ridge-transform-ridge system is determined based on temperature- and pressure-dependent viscosity laws. We consider six transform lengths, spanning 0 to 250 km in increments of 50 km. We then calculate the 3-D viscous flow in response to an along-axis pressure gradient corresponding to a ridge-centered hot spot. Modeling results predict that transform faults affect along-axis asthenospheric flow in two important ways. First, transforms reduce along-axis flux. The longer the transform offset, the greater the reduction in across-transform flux relative to the zero-offset case. Second, transforms deflect shallow asthenospheric along-axis flow. The predicted transform damming effect is most pronounced for a viscosity structure that is strictly pressure- and temperature-dependent. Flux reduction effects could be less significant for viscosity laws that additionally consider dehydration, melting, and change in deformation mechanism. This model predicts that the waist width of an on-axis plume is dependent not only on such previously explored factors as buoyancy and spreading rate, but also on the geometry of ridge segmentation. Along the SWIR, axial flow driven by the Marion plume is likely curtailed by the long-offset Andrew Bain and Discovery II fracture zones, severely limiting its lateral extent.

Components: 7939 words, 11 figures, 2 tables.

Keywords: Mantle plumes; transform faults; Southwest Indian Ridge; Marion hot spot.

Index Terms: 3035 Marine Geology and Geophysics: Mid-ocean ridge processes.

Received 5 March 2003; **Revised** 2 July 2003; **Accepted** 15 July 2003; **Published** 11 September 2003.

Georgen, J. E., and J. Lin, Plume-transform interactions at ultra-slow spreading ridges: Implications for the Southwest Indian Ridge, *Geochem. Geophys. Geosyst.*, *4*(9), 9106, doi:10.1029/2003GC000542, 2003.

Theme: Accretionary Processes Along the Ultra-Slow Spreading Southwest Indian Ridge
Guest Editors: Catherine Mevel and Daniel Sauter

1. Introduction

[2] A significant portion of the mid-ocean ridge system is influenced by mantle plumes [*Schilling*, 1991]. Near- or on-ridge plumes thicken oceanic crust, alter mid-ocean ridge geochemistry, and impart a strong signal to seafloor bathymetry, gravity, and geoid. Numerous investigations have suggested that transform faults influence the distribution of plume material, including the Charlie Gibbs FZ for the Iceland hot spot [*Vogt and Johnson*, 1975] and the Agulhas FZ for the Discovery hot spot [*Douglass et al.*, 1995]. The influence of ridge offsets on plume dispersal was first explored analytically by *Vogt and Johnson* [1975] and *Vogt* [1976]. However, the interaction between plume-driven flow and transform faults has only recently been addressed by numerical geodynamic models [e.g., *Sleep*, 1996]. While most of the recent plume-ridge numerical experiments generally consider straight ridges, the modeling study of *Yale and Phipps Morgan* [1998] predicts strong focusing of Kerguelen plume flow toward a segment of the Southeast Indian Ridge that is offset in the direction of Kerguelen, suggesting that ridge segmentation is important in plume-ridge interaction.

[3] Segmentation is a first-order feature of mid-ocean ridges. Ridges of all spreading rates are segmented, although segmentation patterns and the associated mantle dynamics vary with spreading rate [e.g., *Macdonald*, 1982; *Schouten et al.*, 1985; *Lin and Phipps Morgan*, 1992]. Figure 1 shows the high degree of segmentation along the central portion of the ultra-slow spreading Southwest Indian Ridge (SWIR) near the Marion hot spot. Along the SWIR between 25°–45°E, the Andrew Bain and other transform faults cumulatively offset the SWIR by ~1500 km. The transform effect on along-axis plume flow is likely to be pronounced along the SWIR because of both particularly long transform offset lengths and large lithospheric thickness contrasts across transforms due to the ultra-slow spreading rate.

[4] In this study we use a hybrid finite difference/finite element 3-D numerical model to quantify the role of transform offsets in limiting the along-axis asthenospheric flow driven by a ridge-centered plume. We focus on the SWIR as an end-member case where such a transform effect is likely to be pronounced. We quantify the transform damming effect for six offset lengths, which are relevant to the range of transform lengths observed along the SWIR. We then examine the sensitivity of the transform effect to mantle viscosity structure and discuss the implications of model results for plume-ridge interactions.

2. Numerical Method

[5] We model mantle flow along a segmented ridge driven by a plume-related pressure gradient. The model box is comprised of two segments, each of length L_s, and an intervening transform of length L_t (Figure 2; see Table 1 for definition of model variables). We examine values of L_t ranging from 0 to 250 km in increments of 50 km, overlapping a wide range of offset lengths observed along the SWIR. Computational limitations and model resolution considerations prohibit exploration of offsets significantly greater than 250 km, for which only qualitative results are inferred from extrapolation. The model box is 750 km in the across-axis direction (X), 500 km in the along-axis direction (Y), and 660 km in depth (Z) to coincide with the 660 km mantle discontinuity. A half-spreading rate, U, of 0.75 cm/yr was chosen to reflect the opening rate of the ultra-slow spreading SWIR near the Marion plume.

[6] Numerical calculations are performed in two steps: (1) We calculate three-dimensional (3-D)

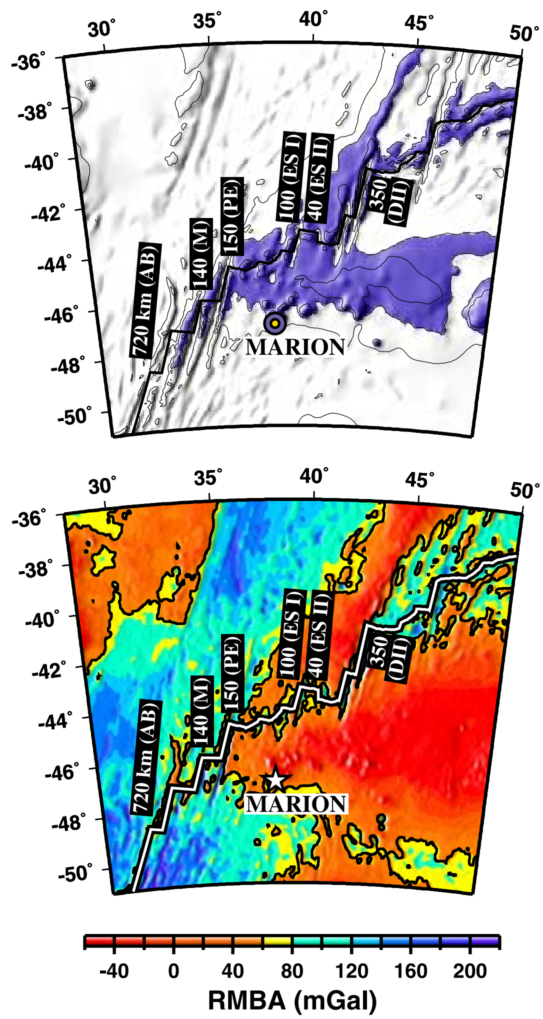

Figure 1. (a) Bathymetric map of the Southwest Indian Ridge in the vicinity of the Marion hot spot, with depths less than 2.75 km shaded. Fracture zones abbreviations are AB, Andrew Bain FZ; M, Marion FZ; PE, Prince Edward FZ; ES, Eric Simpson FZ; and DII, Discovery II FZ. Transform offset lengths are indicated in km, rounded to the nearest 10 km. Contours are drawn at 1.75, 2.75, and 3.75 km depth. Bathymetry data are extracted from *IOC* [1997]. (b) Residual mantle Bouguer anomaly (RMBA) in the vicinity of the Marion hot spot. RMBA reflects subsurface density anomalies, with lower RMBA likely associated with thickened crust and/or lower mantle density. Details of the RMBA calculation are provided in *Georgen et al.* [2001].

viscosity structure for a given L_t using the approach of *Shen and Forsyth* [1992]; and (2) we use this 3-D viscosity structure as input to a fluid dynamical calculation, in which a pressure gradient dP/dY, which simulates an on-axis plume, drives flow along-ridge in the Y-direction. This two-step approach significantly simplifies modeling complexity and enables us to isolate the purely geometrical effects of viscosity structure on the along-axis mantle flow. Our solutions are for the instantaneous interaction between along-axis flow and a transform offset and thus are not designed to investigate the time-dependent evolution of the plume-ridge system. Feedbacks between temperature, viscosity, and velocity fields, which were neglected in the present models, are expected to change the results quantitatively. For example, flow away from a thermal plume will advect high-temperature material, reducing viscosities and thinning the lithosphere. As the anomalously warm plume material approaches a transform, it is likely that relatively high viscosities near the offset will be reduced, and the transform will experience a form of "thermal erosion" [*Vogt and Johnson*, 1975] that was not considered in the present model. In this way, the transform would present less of a barrier to along-axis flow than in the present study.

[7] Pressure- and temperature-dependent viscosity is calculated using a hybrid, iterative finite element/finite difference approach [*Shen and Forsyth*, 1992]. First, the velocity field for incompressible mantle flow driven by passive plate separation is determined using a finite element code with successive overrelaxation. Then, upwind finite differences are used to solve for the mantle temperature field in the model box, assuming $T_{Z=200\ km}$ = 1350°C and $T_{Z=0\ km}$ = 0°C. Viscosity is calculated at each node according to pressure and temperature. Finally, velocity, temperature, and viscosity calculations are iterated until a stable steady state solution is reached. The *Shen and Forsyth* [1992] code has been benchmarked against the analytical flow solutions of *Reid and Jackson* [1981] (Y. Shen, personal communication, 2003). The average upwelling rate predicted by *Shen and Forsyth* [1992] is 97% of the theoretical value $(2/\pi)*U$, with the most significant deviation from the analytical solutions occurring within one grid node of the ridge axis.

[8] The governing equation for viscosity is given by

$$\eta = A\ \sigma^{1-n} \exp[(E + PV)/RT] \qquad (1)$$

where A is a pre-exponential constant, n is the stress exponent, E is activation energy, P is pressure, V

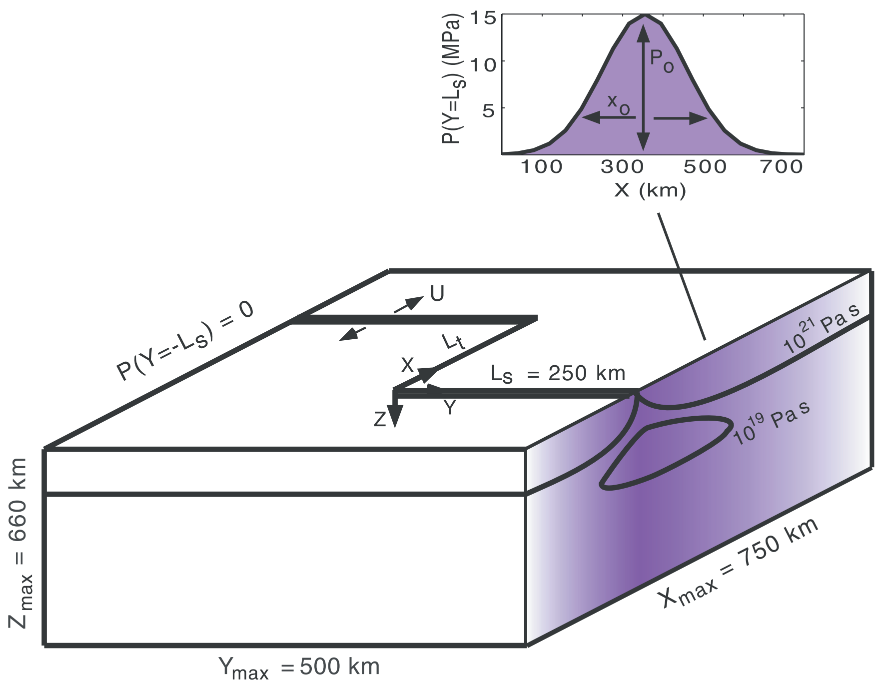

Figure 2. Set-up of the model domain. Two ridge segments, indicated by double lines and each of length L_s = 250 km, are offset by a transform fault of length L_t. Our experiments examine L_t ranging from 0 km to 250 km in increments of 50 km. Half-spreading rate, U, is set to 0.75 cm/yr in the numerical experiments. The model box is X_{max} = 750 km in the spreading direction, Y_{max} = 500 km in the along-axis direction, and Z_{max} = 660 km in depth. A pressure gradient is imposed by applying $P(x) = P_o \exp[-0.5^* (X/X_o)^2]$ at $Y = L_s$ and $P = 0$ at $Y = -L_s$. This pressure gradient drives viscous flow. As shown by shading, the spatial distribution of pressure follows a Gaussian distribution, with maximum amplitude P_o = 15 MPa at the ridge and standard deviation width X_o = 100 km. The locations of the 10^{19} Pa s and 10^{21} Pa s viscosity contours are schematically indicated. Other boundary conditions are zero slip at Z = 0 km and $Z = Z_{max}$, $v_z = 0$ at $Z = Z_{max}$, and zero normal stress at Z = 0 km and the ridge-plane-parallel surfaces of the model box. In calculating viscosity structure, temperature is set to be 0°C at Z = 0 km and 1350°C at $Z \geq 200$ km.

is activation volume, R is the universal gas constant, and T is temperature (Table 1). We set n = 1 (Newtonian fluid) for all calculations, yielding a reference minimum viscosity $\eta_{min} = 10^{19}$ Pa s. Viscosity varies by ~5 orders of magnitude over the model space. Low viscosity values are predicted for a broad depth range with viscosity minima occurring at a depth of approximately 70–75 km (Figure 3a). In plan view, the region of lowest viscosity forms a continuous meandering band along-axis (Figure 3b). Figure 3c shows that the region of lowest viscosity is predicted to take a roughly triangular shape in across-axis section. Further details of the viscosity modeling calculations can be found in *Shen and Forsyth* [1992].

[9] The 3-D viscosity field for each L_t is then used as input to a finite element fluid dynamical code (ADINA [*Bathe*, 1996]) that solves the equation of continuity for an incompressible fluid

$$\nabla \cdot \mathbf{v} = 0 \tag{2}$$

and the equation of momentum balance

$$\nabla P = \nabla \cdot (\eta \nabla \mathbf{v}) + \rho \mathbf{g} \tag{3}$$

with no heat transfer and no buoyancy-driven flow, where **v** is velocity vector, P is fluid pressure, η is viscosity, ρ is mantle density, and **g** is the acceleration of gravity. The driving force for fluid flow is an along-axis pressure gradient dP/dY created by imposing pressure with a Gaussian spatial distribution at $Y = L_s$ and zero pressure at $Y = -L_s$ (Figure 2). The pressure at $Y = L_s$ is

Table 1. Model Parameters

Variable	Meaning	Value	Units
E	Activation energy	520	kJ/mol
V	Activation volume	10×10^{-6}	m^3/mol
n	Stress exponent	1	
η_{min}	Minimum viscosity	10^{19}	Pa s
ρ	Mantle density	3300	kg/m^3
g	Gravitational acceleration	9.8	m/s^2
$\mathbf{g}$	Gravity vector		
R	Universal gas constant	8.3144	J/mol·K
$T_{z=0\ km}$	Surface temperature	0	°C
$T_{z=200\ km}$	Mantle temperature	1350	°C
K	Thermal diffusivity	10^{-6}	m^2/s
X	Distance in spreading direction		km
X_{max}	Box length, spreading direction	750	km
Y_{max}	Box length, along-axis direction	500	km
D_{stag}	Distance of velocity stagnation point from plume origin		km
Z	Depth below surface		km
Z_{max}	Box depth	660	km
L_s	Segment length	250	km
L_t	Transform length	0, 50, 100, 150, 200, 250	km
U	Half-spreading rate	0.75	cm/yr
$\mathbf{v}$	Velocity vector		cm/yr
v_x	Velocity in spreading direction		cm/yr
v_y	Along-axis velocity		cm/yr
v_z	Vertical velocity		cm/yr
Q	Along-axis volumetric flux		km^3/yr
P	Pressure		Pa
P_o	Maximum pressure at Y = L_s	15	MPa
X_o	Pressure Gaussian width	100	km

assumed to be maximum at the ridge axis with an across-axis distribution given by

$$P(X) = P_o \exp\left[-0.5^*(X/X_o)^2\right], \qquad (4)$$

where P_o is the maximum pressure and X_o is the Gaussian distribution standard deviation width. Other boundary conditions are zero slip at Z = 0 km and $Z = Z_{max}$, $v_z = 0$ at $Z = Z_{max}$, and zero normal stress at Z = 0 km and the ridge-plane-parallel surfaces of the model box. Along-axis flux Q of mantle material is defined as

$$Q(Y) = \int v_y \, dX \, dZ \qquad (5)$$

where v_y is along-axis velocity (Table 1) and the integration is taken over the entire X-Z plane at constant Y.

[10] Since the along-axis viscous flow scales with dP/dY, it is important to examine in more detail the selection of P_o. The selection of P_o follows two different arguments, relating to plume buoyancy and topographic loading, respectively. First, following *Conder* [2000], we assume that plume-induced differential pressure ΔP scales with buoyancy force:

$$\Delta P \sim \rho\alpha\Delta Tg\Delta L, \text{ or } \Delta P/\Delta L \sim \rho\alpha\Delta Tg \qquad (6)$$

where ρ is reference mantle density, ΔT is plume thermal anomaly, ΔL is upwelling length, and α is the coefficient of thermal expansion. If we assume that ρ = 3300 kg/m^3, $\alpha = 3 \times 10^{-5}$ K^{-1}, and g = 9.8 m/s^2, the scaling relation of Equation (6) becomes $\Delta P/\Delta L \sim \Delta T$. For the on-axis Iceland plume, models suggest $\Delta T \sim 50–200$ K [*Ito et al.*, 1999], yielding $\Delta P/\Delta L \sim 50–200$ kPa/km. This is probably an upper limit for plume-related along-axis pressure gradients. $\Delta P/\Delta L$ will be smaller for off-axis plumes and plumes with smaller ΔT. Two recent studies have modeled asymmetric flow across the axis of the East Pacific Rise, assuming that mantle flow is driven by the distant Pacific Superswell [*Phipps Morgan et al.*, 1995]. *Conder et al.* [2002], for example, assume $\Delta P/\Delta L \sim 1–10$

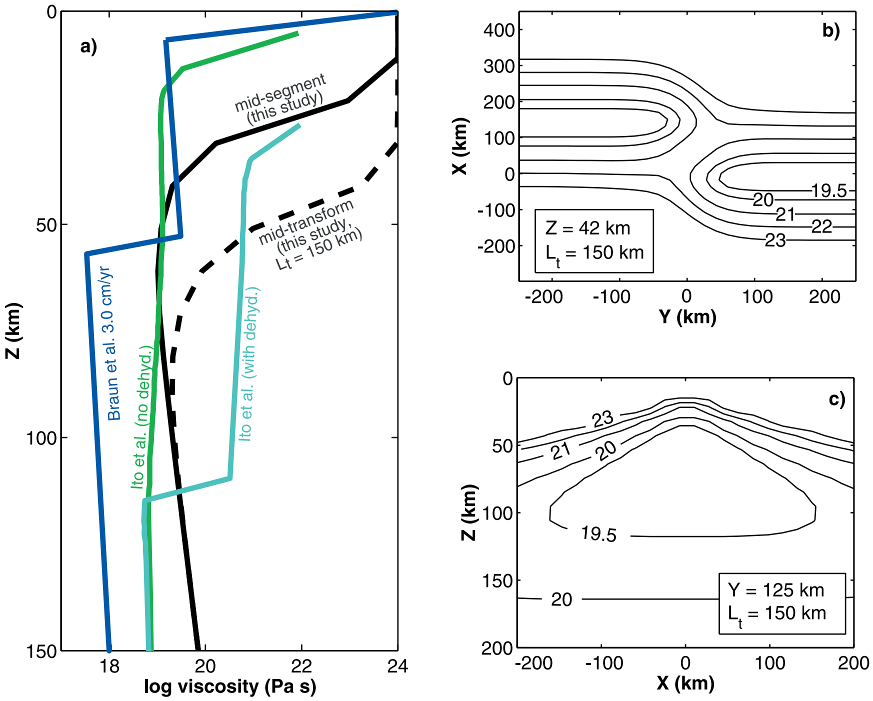

Figure 3. (a) Viscosity-depth profiles for the top 150 km of the model space. Black lines show profiles from this study, taken at the midpoint of a ridge segment (solid line) and the midpoint of a transform with L_t = 150 km (dashed line). All of our models in panels a–c are for U = 0.75 cm/yr. Additional profiles (colored lines) show viscosity-depth profiles from other modeling studies for reference. The profile labeled "Braun et al. 3.0 cm/yr" (blue line) shows a mid-segment profile for U = 3.0 cm/yr when considering the effects of not only pressure and temperature but also dehydration, melting, and deformation mechanism [*Braun et al.*, 2000]. *Braun et al.* [2000] assume a mantle potential temperature of 1350°C at 660 km. Note that the *Braun et al.* [2000] solution predicts a high-viscosity lid extending to depths of ~60 km, the transition from dry to damp melting. In contrast, *Ito et al.* [1999], who also consider the effects of dehydration on viscosity, place the boundary of wet and dry melting at approximately 110 km (cyan curve). The *Ito et al.* [1999] viscosity-depth profile is taken through the center of a ridge-centered plume. The maximum hot spot mantle potential temperature was assumed to be 1530°C for Z > 240 km, half-spreading rate was 0.95 cm/yr, and viscosity was 3.5 × 10^{19} Pa s at 200 km depth. For comparison, the *Ito et al.* [1999] viscosity-depth profile without dehydration is plotted in green. (b) Viscosity slice at Z = 42 km for L_t = 150 km. Viscosity contours are in Pa s. (c) Across-axis viscosity slice at Y = 125 km.

kPa/km. Likewise, *Toomey et al.* [2002] use a pressure gradient of 2 kPa/km.

[11] If mantle flow is driven by topographic loading of a lithospheric plate by emplacement of a volcanic edifice, ΔP should scale as

$$\Delta P \sim \rho g \Delta h, \text{ or } \Delta P/\Delta L \sim \rho g \Delta h/\Delta L \qquad (7)$$

where Δh is elevation of the topographic anomaly relative to the surrounding seafloor and ρ = 2700 kg/m^3. On the basis of the plateau heights of the Galapagos, Azores, and Iceland hot spots, Δh/ΔL is approximately 0.8/500, 4/1300, and 1.8/1100 km/km [*Ito and Lin*, 1995], respectively, yielding ΔP/ΔL ~ 42, 43, and 81 kPa/km. The topographic anomaly for Marion is less straightforward to define than for these other hot spots [*Georgen et al.*, 2001], but a best estimate for ΔP/ΔL for Marion is approximately 30–40 kPa/km. Thus in this study we assign P_o = 15 MPa, yielding an along-axis pressure gradient $\Delta P/\Delta L = P_o/Y_{max}$ = 15 MPa/500 km = 30 kPa/km. Note that the resultant along-axis plume velocity is scaled proportionally to the assumed ΔP/ΔL.

[12] While our model assumes a depth-independent pressure gradient focused on the ridge, other spatial distributions and types of driving forces associated with a mantle plume may also give rise to along-axis mantle flow. For example, a pressure that

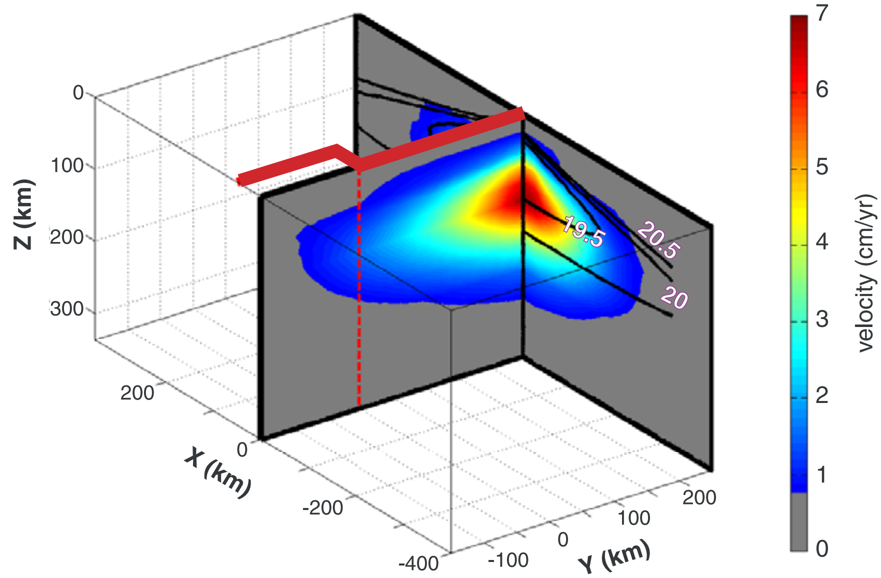

Figure 4. Selected slices of flow velocity through the model domain, for L_t = 50 km. Ridge geometry is indicated by thick red lines, and the vertical projection of the transform offset is shown by a dotted red line. Viscosity contours (black lines) are labeled in $\log_{10}$ Pa s, with a contour interval of 0.5.

decreases with depth may reflect a hot spot whose origin is a relatively shallow geochemical anomaly with vertical extent much less than 660 km. Alternatively, along-axis flow may be driven by upwelling and dispersal of a buoyant plume. However, such buoyancy driving forces are unlikely to yield qualitatively significantly different flow results than the pressure configuration used here. For example, *Ito et al.* [1996] modeled the dispersion of a buoyant Iceland plume along the Mid-Atlantic Ridge. Qualitative comparison of the along-axis velocity results from *Ito et al.* [1996] and this study shows that the depths and across-axis extents of the region of fast along-axis flow are quite similar, despite differences in the magnitude of the flow because of the unusually large flux of the Iceland plume. This confirms that the shallowly rooted, buoyancy-driven plumes should yield the same qualitative flow structure as the depth-independent pressure gradient considered here because in both cases nearly all flow occurs in the low-viscosity region in the upper 200 km of the model space.

[13] The computational grid for viscosity structure is 41 × 30 × 19 nodes, yielding grid spacing of 18.8 × 17.2 × 10.5 km. Viscosity is calculated for a box with dimensions $X_{max} \times Y_{max} \times 200$ km, and padded to a depth of 660 km by extrapolation according to pressure-depth relationships. A slightly different nodal grid of 41 × 25 × 21 is used for the flow velocity calculations. This results in spatial resolution of 18.8 × 20.8 km in the X and Y directions, respectively, and variable spacing, from 6 to 60 km, in Z with highest resolution near the surface where vertical gradients in viscosity are greatest. Benchmark calculations for an isoviscous channel-flow problem yield numerical results that differ by <1% from analytical solutions.

3. Results

[14] The presence of a transform offset is calculated to have two general effects on along-axis flow, (1) deflection of shallow mantle flow toward the offset direction and (2) reduction in mantle flux across the transform. We discuss these two effects below.

3.1. Deflection of Shallow Mantle Flow

[15] In across-axis section, the high-velocity region forms the shape of a flattened triangle (Figure 4), following viscosity contours (Figure 3c). For the prescribed along-axis pressure gradient of 15 MPa over 500 km ($\Delta P/\Delta L$ = 30 kPa/km), the maximum

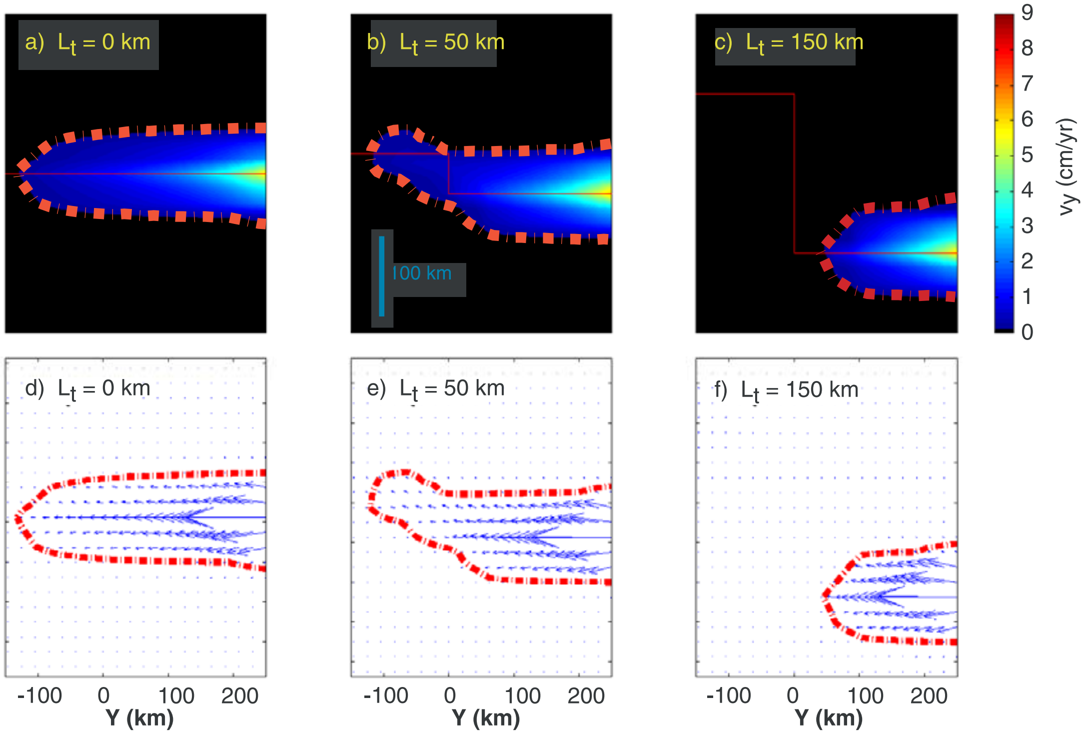

Figure 5. (top) Plan view slices of along-axis velocity at Z = 72 km, for L_t = 0, 50, and 150 km (Figures 5a, 5b, and 5c, respectively). Red lines indicate ridge-transform-ridge geometry. Note the clear deflection of the region of high along-axis velocity for L_t = 50 km (Figure 5b). Note also that the region of high along-axis velocity stops farther upstream from the transform as offset increases (compare Figures 5a and 5c). Dash-dot red line indicates the contour for v_y = 0.125 cm/yr. (bottom) Flow vectors at Z = 72 km, for L_t = 0, 50, and 150 km (Figures 5d, 5e, and 5f, respectively). Dash-dot red line indicates the contour for v_y = 0.125 cm/yr.

along-axis velocity, $v_{y\ max}$, is ~10 cm/yr for the zero transform offset case, significantly faster than the spreading rate. These high velocities are achieved at a depth of approximately 75 km, where minima in viscosity-depth profiles are reached (Figure 3a).

[16] In plan view, the region of high along-axis velocity forms a band around the ridge axis, again following viscosity contours (Figure 5). Owing to flow in the spreading (X) and vertical (Z) directions, the along-axis flux Q decreases as a function of decreasing Y even in the absence of a transform fault (i.e., for L_t = 0 km) (Figures 5a and 5d). For the zero transform offset case, for example, the calculated flux decreases from Q = 2.5 km^3/yr at Y = L_s to Q = <1 km^3/yr at Y = 0, corresponding to ~60% reduction in Q over a distance of L_s (Figure 6). Within the zone of fastest along-axis flow at the depth of 72 km, the along-axis velocity decreases from $v_{y\ max}$ at Y = L_s to 0.185 * $v_{y\ max}$ at Y = 0.

[17] Along-axis flow stagnates farther upstream from the transform as the transform offset increases (Figure 5). Comparison of Figures 5a and 5c shows that high values of v_y are more restricted for L_t = 150 km than for L_t = 0 km. Similarly, Figure 7 shows that v_y at 72 km depth for L_t = 150 km is reduced relative to the case of L_t = 0 km. Along-axis velocity for L_t = 150 km begins to significantly decrease, compared to L_t = 0 km, approximately 100 km from the transform offset.

[18] Figure 8 quantifies decreases in along-axis velocity for all L_t. We define D_{stag} as the distance from the edge of the model box at Y = L_s to where the along-axis velocity is reduced to v_y = 0.185 * $v_{y\ max}$ at a depth of Z = 72 km. For zero transform offset (L_t = 0 km), D_{stag} = L_s. Figure 8 suggests that the longer the offset, the farther upstream from the transform fault the high-velocity flow is predicted to stop. For example, D_{stag} ~ 0.83 L_s for L_t = 50 km, but D_{stag} reduces to 0.67 L_s for $L_t \geq$ 150 km.

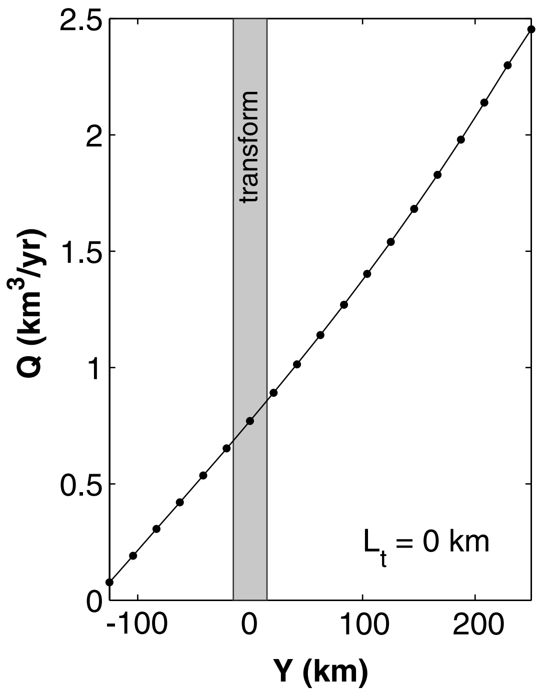

Figure 6. Along-axis volumetric material flux Q through vertical planes perpendicular to the spreading axis, for the case of $L_t = 0$. Note that flux decreases in the along-axis direction away from the plume pressure center at $Y = L_s = 250$ km, even without a transform offset, because of material flow in the spreading (X) and vertical (Z) directions.

[19] In addition to impeding along-axis flow, transform offsets may also deflect it in the direction of the next ridge segment. Such deflection can be seen for the case of $L_t = 50$ km (Figures 5b and 5e), where the region delineated by $v_y = 0.125$ cm/yr persists across the transform. This effect is not clearly visible for greater L_t, however, because of the stagnation effect described above.

3.2. Reduction in Flux Across a Transform Fault

[20] Figure 9 shows the relationship between transform offset length and along-axis flux reduction, using normalized flux, $Q/Q_{Lt=0}$. The presence of a transform fault is predicted to reduce Q along the entire length of the ridge axis, both upstream ($Y > 0$ km) and downstream ($Y < 0$ km) of the transform fault. For example, for the case of $L_t = 250$ km (Figure 9), the calculated $Q/Q_{Lt=0}$ at $Y = 100$ km is $\sim$0.8, indicating that flux is already noticeably reduced upstream of the transform. This upstream flux reduction occurs because model viscosity increases gradually along-axis at all depths as the transform is approached. For large transforms, the increased viscosity due to thermal cooling around the transform fault is predicted to extend for a relatively long distance along-axis. Downstream from the transform fault, the spatial gradient in the reduction of Q is even greater. As a result, the calculated along-axis material flux Q is essentially zero within 100 km downstream of the transform for large L_t (Figure 9). In general, the fluxes are predicted to decrease by a greater amount for larger L_t. For example, for $L_t = 250$ km, flux across the transform ($Y = 0$ km) is predicted to be reduced by 40% relative to the no-transform case, whereas for $L_t = 50$ km, this flux reduction is only $\sim$10%.

4. Alternative Viscosity Models

[21] The modeling results discussed so far are for viscosity that varies only as a function of temperature and pressure. However, viscosity may also be influenced by other factors including the presence of melt, dehydration during melting, and transitions in creep mechanism [*Hirth and Kohlstedt*, 1995a, 1995b, 1996; *Phipps Morgan*, 1997; *Braun et al.*, 2000]. Numerical models of *Braun et al.* [2000] yield the following general predictions. (1) Latent

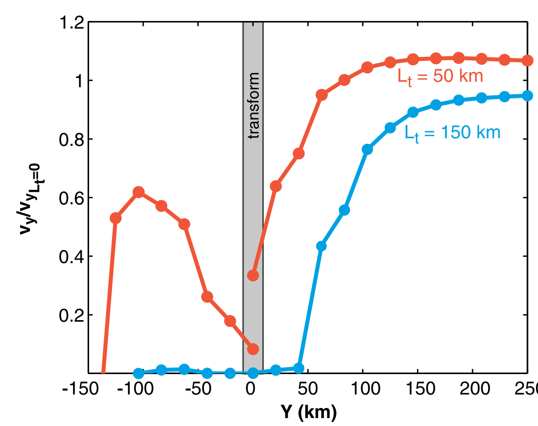

Figure 7. Along-axis velocity, v_y, for $L_t = 50$ and $L_t = 150$ km at 72 km depth, as a function of along-axis distance. Profiles are normalized to the case of $L_t = 0$ km. Discontinuities in the profiles occur at the transform fault ($Y = 0$ km) because velocities were extracted only along the two ridge axes, which are offset by the transform fault.

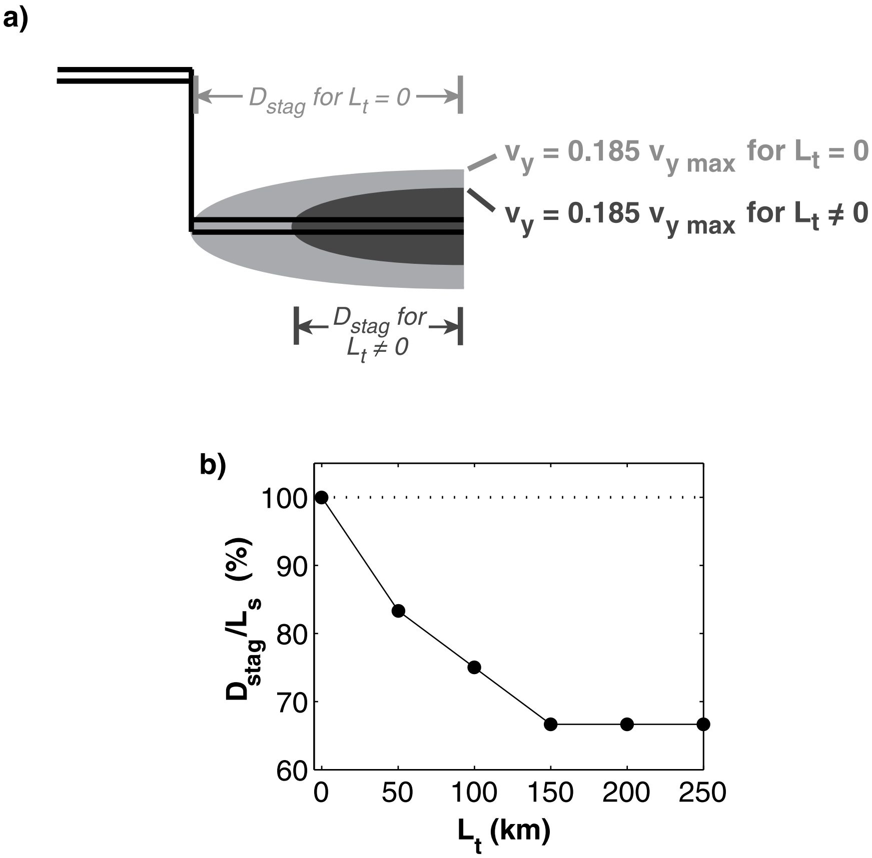

Figure 8. The effect of a transform fault on the calculated location of a velocity stagnation point at depth of Z = 72 km (within the zone of fastest along-axis flow). (a) D_{stag} is the distance from the edge of the model box (at Y = L_s) to where the along-axis velocity is reduced to $v_y = 0.185\ v_{y\ max}$. For zero transform offset (L_t = 0 km), $D_{stag} = L_s$. (b) Normalized stagnation distance plotted as D_{stag}/L_s. Note that the longer the transform offset, the farther upstream from the transform is the stagnation point.

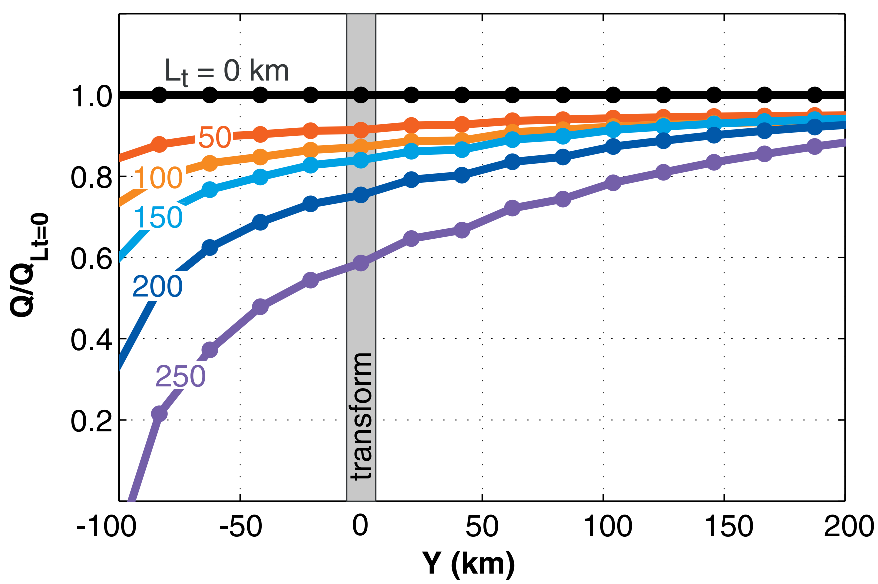

Figure 9. Normalized flux $Q/Q_{Lt\ =\ 0}$ as a function of along-axis distance. Normalized flux curves are given for all six L_t, ranging from 0 km to 250 km. The transform offset is located at Y = 0 km. Note that flux at all locations decreases with increasing transform length L_t. Downstream from the transform fault (Y < 0), the reduction in the flux is even greater.

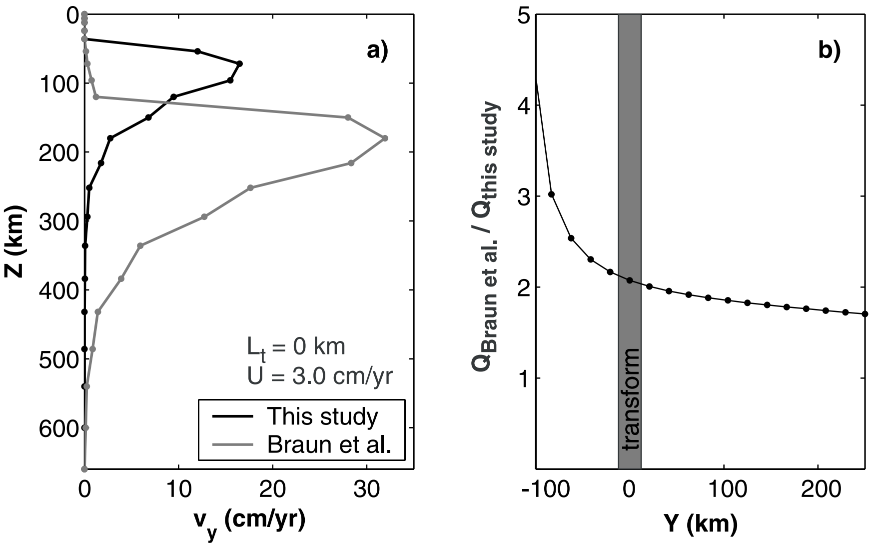

Figure 10. (a) A comparison of predicted axial velocity-depth profiles calculated using strictly pressure- and temperature-dependent viscosities (this study, black line) and the viscosity solution of *Braun et al.* [2000] (gray line), which considers the additional effects of melting, dehydration, and change in deformation mechanism. Velocity profiles were taken at X = 0 km and Y = L_s = 250 km, for L_t = 0 km and U = 3.0 cm/yr. (b) A comparison of along-axis flux calculated using the viscosity solutions of this study and *Braun et al.* [2000], plotted as the ratio of the two solutions.

heat changes during melting affect viscosity relatively little, increasing it at the depths where dry melting occurs by less than an order of magnitude compared to strictly temperature- and pressure-dependent viscosity. (2) The retention of a small amount of melt in the mantle matrix (e.g., ~3%) also has a relatively small effect, decreasing the shallow mantle viscosity by less than an order of magnitude. (3) Dehydration during melting is suggested to increase viscosity by approximately two orders of magnitude in the shallow mantle. (4) Transition in creep mechanism results in a viscosity decrease of an order of magnitude. The predicted combined effect of all four of these processes is to cause a maximum increase in viscosity in the dry melting regime (shallow depths) of approximately an order of magnitude, and a maximum decrease in viscosity in the wet melting regime (greater depths) of approximately an order of magnitude. This effect can be seen in Figure 3a, where the *Braun et al.* [2000] viscosity-depth curve for 3.0 cm/yr has a pronounced step at a depth of ~60 km, approximately the depth of the transition from damp to dry melting.

[22] To assess the potential effects of melting, dehydration, and transition in creep mechanism on along-axis velocity, we computed 3-D flow fields using the viscosity structure predicted by *Braun et al.* [2000] for a single ridge with U = 3.0 cm/yr, and compared the results to the flow fields predicted for a strictly pressure- and temperature-dependent viscosity structure, also with U = 3.0 cm/yr. It was necessary to use this intermediate spreading rate, rather than the ultra-slow rate used in the rest of the model runs, because *Braun et al.* [2000] did not model U = 0.75 cm/yr. Nevertheless, the results are qualitatively applicable to the U = 0.75 cm/yr case. Also, since *Braun et al.* [2000] only examined a 2D, axis-perpendicular geometry, we repeated their viscosity-depth solution along-axis to generate a 3-D viscosity structure with no transform offsets. We adjusted the minimum viscosity used by *Braun et al.* [2000] to match $\eta_{min} = 10^{19}$ Pa, the minimum viscosity in the present study.

[23] Flow fields calculated using the Braun et al. viscosity structure differ from those predicted using strictly pressure- and temperature-dependent viscosity in several important ways (Figure 10). For example, while maximum v_y for the strictly pressure- and temperature-dependent viscosity solution occurs at a depth less than 100 km, the maximum v_y for the

equalized Braun et al. viscosity structure is found at a depth slightly less than 200 km (Figure 10a). Moreover, maximum v_y for the Braun et al. solution is greater (>30 cm/yr) than that for the strictly pressure- and temperature-dependent viscosity solution ($\sim$15 cm/yr) for the same imposed along-axis pressure gradient (Figure 10a). The calculated Q for the Braun et al. viscosity structure is roughly twice that of the strictly pressure- and temperature-dependent solution upstream of the transform (Y > 0 km), but is more than 4 times that of the strictly pressure- and temperature-dependent solution downstream of the transform (at $Y \sim -100$ km) (Figure 10b), indicating that plume-driven flow can travel longer distances along-axis for the Braun et al. viscosity structure. Because more flow can be accommodated at greater depth for the Braun et al. model than the strictly pressure- and temperature-dependent model, the shallow transform damming effect is predicted to be considerably smaller for the Braun et al. viscosity structure.

[24] Clearly, the degree to which transform faults impede along-axis flow is greatly influenced by the choice of 3-D viscosity structure. Since the transform cooling effect is greatest at the surface and decreases with depth, transform fault damming is most pronounced for a viscosity structure in which the depth of minimum viscosity is comparable to lithospheric thickness. Accordingly, the transform damming effect is predicted to be significant for the *Shen and Forsyth* [1992] curve in Figure 3a, where the viscosity minimum occurs at a depth of $\sim$75 km, which is comparable to the thickness of cold lithosphere. In contrast, for the same transform length, the transform damming effect is predicted to be significantly smaller for viscosity-depth curves including dehydration [e.g., *Ito et al.*, 1999], because the entirety of the upper $\sim$110 km of the mantle has high viscosity. In the model of *Ito et al.* [1999], plume material spreads horizontally at depth, and flow is not preferentially channeled along-axis. However, *Ito et al.* [1999] have noted that their calculated dehydration viscosities are somewhat higher than viscosities derived from postglacial rebound and post-seismic deformation studies [*Sigmundsson and Einarsson*, 1992; *Pollitz and Sacks*, 1996]. Future investigations that employ combined seismic, electromagnetic, and geodetic approaches are needed to provide improved constraints on the in situ viscosity structure beneath mid-ocean ridge systems.

5. Discussion: Implications for Plume-Ridge Interactions

5.1. Marion Hot Spot and Its Interactions With Ultra-Slow Spreading SWIR

[25] The results of this modeling study can be used to explore how ridge segmentation affects the along-axis length of plume-generated geochemical/geophysical anomalies, or waist width W. The ultra-slow spreading SWIR is highly segmented in the vicinity of the Marion hot spot (Figure 1a). *Georgen et al.* [2001] use ship track bathymetry data, free-air gravity, residual gravity anomalies (RMBA), and limited available geochemical data to investigate Marion's waist width. Although precise definition of the length of Marion-affected SWIR is made difficult by short-wavelength, segment-scale variations, *Georgen et al.* [2001] point out that the along-axis influence of the Marion hot spot is most prominent between the Andrew Bain and Discovery II FZs (Figure 1a, and additional figures in *Georgen et al.* [2001]). Andrew Bain FZ is among the world's longest transform offsets, with a length of $\sim$720 km, while Discovery II FZ is a dual fracture zone system with a combined offset of approximately 350 km.

[26] To apply the numerical results obtained in this study to the SWIR, we assume that the Marion plume drives mantle flow from Marion Island to the SWIR axis near the Eric Simpson FZ, and the flow then disperses along-axis to both sides of the Eric Simpson FZ. To the east, the first fracture zone encountered by the hypothesized along-axis flow is Discovery II. Extrapolation of the results in Figure 9 predicts that the reduction in along-axis flux for the 350-km long Discovery II system should be much greater than 40%, which is the calculated flux reduction for the L_t = 250 km case (Table 2). Moreover, within a distance of <100 km beyond the transform, Q is predicted to diminish to 0% (Figure 9). Therefore modeling results predict that the along-axis geophysical expression of the

Table 2. Predicted Flux Reduction Across Central SWIR Transform Faults

Transform Fault	Offset, km	Predicted Flux Reduction Across Transform
Discovery II	350	>40%
Eric Simpson II	40	~10%
Eric Simpson I	100	~15%
Prince Edward	150	~20%
Marion	140	~20%
Andrew Bain	720	>40%

Marion plume would terminate in the vicinity of the Discovery II FZ. A similar argument applies for the westernmost boundary of the Marion axial anomaly. The Andrew Bain FZ, with an offset length approximately twice as long as that of Discovery II, is predicted to effectively block all westward asthenospheric flow.

[27] Geophysical data qualitatively support the transform-limited Marion plume dispersal model. Bathymetric surveys of the segment between the Andrew Bain and Marion FZs, as well as the segment between the Marion and Prince Edward FZs, reveal more robust magmatism than would be expected for an ultra-slow spreading ridge [*Grindlay et al.*, 1996, 1998, 2000]. This observation supports the hypothesis that the relatively short offsets of the Marion and Prince Edward FZs are not sufficient to curtail Marion-driven along-axis flow. In contrast, the large offset Andrew Bain is sufficient to limit the Marion bathymetric and gravity anomalies as noted above (Figure 1). Geochemical substantiation of Marion's waist width is difficult at present because of wide sample spacing. However, as new geochemical data become available, they will provide valuable additional constraint on Marion's interaction with the SWIR, and better illustrate the extent to which transforms control Marion dispersion.

[28] The mantle flow field beneath the SWIR near the Marion hot spot could consist of two components, i.e., the pipe-like along-axis flow discussed above, and radial flow directly from the hot spot. Because the segments bordering the Prince Edward and Marion FZs are relatively close to Marion, it is plausible that some mantle material may flow directly to these ridge segments from the hot spot. Radial flow may therefore contribute to the excess volcanism and shallow bathymetry observed along this portion of the SWIR. However, such direct flow from Marion to the more distant ridge segments near the Discovery II FZ could be far less. The existing observational constraints are still far too limited to distinguish the relative contribution of pipe-like along-axis flow versus radial plume dispersion in such a complex system, highlighting the need for comprehensive on- and off-axis investigations in the future.

[29] The qualitative agreement between geophysical observations and model predictions in the vicinity of the Marion hot spot also has implications for the nature of upper mantle viscosity structure. As discussed above, models that employ a more complex viscosity structure, including dehydration, melting, and changes in deformation mechanism, predict that plume-driven flow should occur at relatively great depths as compared to models that use strictly temperature- and pressure-dependent viscosity. As a result, the transform damming effect is expected to be significantly less for the complex viscosity structure. Thus the apparent sensitivity of geophysical anomalies to ridge offsets in the Marion area is qualitatively consistent with the hypothesis of a relatively shallow low viscosity zone beneath the SWIR axis.

5.2. Plume Waist Width

[30] Results of this study predict that long transform offsets along ultra-slow spreading ridges may strongly localize axial plume anomalies and thus decrease the plume width W relative to the case of an unsegmented ridge. Numerical [*Ribe et al.*, 1995; *Ito et al.*, 1996] and laboratory modeling [*Feighner and Richards*, 1995] suggests that steady state waist width W scales as $W \sim c_o(Q_v/2U)^{1/2}$, where Q_v is plume volume flux and c_o is a scaling coefficient between 1.77 and 2.12, predicting W increases with decreasing spreading rate U. These studies, however, considered only unsegmented ridges and did not take into account the effects of transform offsets. In contrast, our modeling results suggest that in the presence of a transform offset, W will decrease according to transform offset length. The above scaling relationship, therefore,

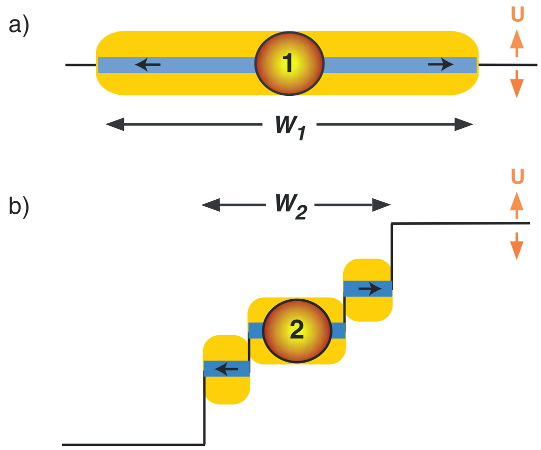

Figure 11. Schematic cartoons of plume-ridge interaction for (a) an unsegmented ridge and (b) a ridge with significant transform offsets. Red circles show plan view of a hypothesized vertical plume conduit. The conduit size and flux of plume 1 are assumed to equal to those of plume 2. The half-spreading rate U is also assumed to be the same. Yellow shading depicts along-axis dispersal of plume material along a low-viscosity pipe, and the ridge axes with a plume signature are emphasized with blue lines. The lengths of the ridges affected by the plumes, or waist width, are W_1 and W_2. Because along-axis flux in b is limited by transform faults, $W_2 < W_1$. Thus flux inferred from waist width will be an underestimate for plume 2 compared to the case of an unsegmented ridge.

may be modified to $W \sim c_o r_o (Q_v/2U)^{1/2}$, where r_o accounts for waist width reduction due to ridge geometry. The value of r_o should be highly dependent on specific ridge configuration with $r_o = 1$ for no transform offset and $r_o = 0$ for a transform fault of infinite offset length. Further numerical modeling work is required to calculate r_o for cases where plume-driven asthenospheric flow crosses multiple transforms with intervening segments of variable length. For example, for the case of the SWIR to the west of the Marion plume, it is likely that reduction in flow occurs across the Marion and Prince Edward FZs prior to reaching the Andrew Bain FZ. Additional modeling work can estimate the cumulative value of r_o for this three-transform system.

[31] The geometric differences between segmented and unsegmented ridges are illustrated in Figure 11. We assume that two plumes, plume 1 and plume 2, have the same flux, and interact with an unsegmented and segmented ridge, respectively. Because along-axis flux is limited by transforms along the segmented ridge (Figure 11b), the apparent waist width W_2 for plume 2 will be less than the waist width W_1 for plume 1. Consequently the flux inferred from waist width for plume 2 will be an underestimate. This illustrates that extra care must be exercised when applying scaling relationships to determine plume flux in a highly segmented environment.

6. Conclusions

[32] The results from this study indicate that transform faults affect plume-driven mantle flow in two important ways:

[33] 1. Transform faults reduce along-axis flux. The degree of flux reduction increases with increasing transform offset length. For example, relative to the case with no transform offset, the along-axis flux is calculated to be reduced by as much as 40% when crossing a transform with offset length of $L_t = 250$ km, for a half-spreading rate of 0.75 cm/yr and strictly pressure- and temperature-dependent viscosity structure. Furthermore, flux decreases rapidly along the segment downstream of the transform, such that for $L_t = 250$ km, the normalized flux is effectively zero within 100 km downstream of the transform.

[34] 2. Transforms deflect shallow asthenospheric along-axis flow toward the direction of the next ridge segment. Moreover, with longer transform offsets, the along-axis flow stops farther upstream of the transform.

[35] The degree to which a transform fault affects plume-driven along-axis asthenospheric flux is sensitive to viscosity structure. The transform damming effect is most pronounced for strictly pressure- and temperature-dependent viscosity, because most flow occurs in a region of low viscosity at the relatively shallow depth of ~75 km, approximately the thickness of cold lithosphere. However, the transform damming is calculated to be less for viscosity structures that additionally include the effects of melting, dehydration, and change in deformation mechanism, since these additional effects result in a thick,

high-viscosity layer extending to depths greater than lithospheric thickness.

[36] Transform offsets in slow- and ultraslow-spreading, highly segmented ridge environments are likely to greatly limit the along-axis dispersion of plume material. Along the Southwest Indian Ridge, axial flow driven by the Marion plume is likely curtailed by the long-offset Andrew Bain and Discovery II fracture zones, severely limiting its lateral extent.

Acknowledgments

[37] We are grateful to Yang Shen for providing computational programs for calculating ridge temperature and viscosity structure and to Mike Braun for providing results of viscosity calculations. This work benefited from discussions with G. Ito, J. Escartin, B. West, Y. Shen, M. Braun, S. Stein, B. Tucholke, M. Behn, R. Detrick, N. Grindlay, and R. Stein and by constructive reviews by Jason Phipps Morgan, Anne Briais, and Daniel Sauter. This work is supported by NSF grants OCE-9811924 and OCE-9907630. Woods Hole Oceanographic Institution contribution number 10487.

References

Bathe, K.-J., *Finite Element Procedures*, 1037 pp., Prentice Hall, Upper Saddle River, N.J., 1996.

Braun, M. G., G. Hirth, and E. M. Parmentier, The effects of deep damp melting on mantle flow and melt generation beneath mid-ocean ridges, *Earth Planet. Sci. Lett.*, *176*, 339–356, 2000.

Conder, J. A., Tectonics and plate boundary processes along the Southeast Indian Ridge and East Pacific Rise, Ph.D. thesis, Brown Univ., Providence, R. I., 2000.

Conder, J. A., D. W. Forsyth, and E. M. Parmentier, Asthenospheric flow and asymmetry of the East Pacific Rise, MELT area, *J. Geophys. Res.*, *107*(B12), 2344, doi:10.1029/2001JB000807, 2002.

Douglass, J., J.-G. Schilling, R. H. Kingsley, and C. Small, Influence of the Discovery and Shona mantle plumes on the southern Mid-Atlantic Ridge: Rare earth evidence, *Geophys. Res. Lett.*, *22*, 2893–2896, 1995.

Feighner, M. A., and M. A. Richards, The fluid dynamics of plume-ridge and plume-plate interactions: An experimental investigation, *Earth Planet. Sci. Lett.*, *129*, 171–182, 1995.

Georgen, J. E., J. Lin, and H. J. B. Dick, Evidence from gravity anomalies for interactions of the Marion and Bouvet hotspots with the Southwest Indian Ridge: Effects of transform offsets, *Earth Planet. Sci. Lett.*, *187*, 283–300, 2001.

Grindlay, N. R., J. Madsen, C. Rommevaux-Jestin, J. Sclater, and S. Murphy, Southwest Indian Ridge 15°E–35°E: A geophysical investigation of an ultra-slow spreading mid-ocean ridge system, *InterRidge News*, *5*, 7–12, 1996.

Grindlay, N. R., J. Madsen, C. Rommevaux-Jestin, and J. Sclater, A different pattern of ridge segmentation and mantle Bouguer gravity anomalies along the ultra-slow spreading Southwest Indian Ridge, *Earth Planet. Sci. Lett.*, *161*, 243–253, 1998.

Grindlay, N. R., J. Madsen, T. Dulaney, and D. Smith, Variations in axial relief and gravity anomalies at the Southwest Indian Ridge 15°E–35°E (abstract), *Geophys. Res. Abstr.*, *2*, 47, 2000.

Hirth, G., and D. L. Kohlstedt, Experimental constraints on the dynamics of the partially molten upper mantle: Deformation in the diffusion creep regime, *J. Geophys. Res.*, *100*, 1981–2001, 1995a.

Hirth, G., and D. L. Kohlstedt, Experimental constraints on the dynamics of the partially molten upper mantle: 2. Deformation in the dislocation creep regime, *J. Geophys. Res.*, *100*, 15,441–15,449, 1995b.

Hirth, G., and D. L. Kohlstedt, Water in the oceanic upper mantle: Implications for rheology, melt extraction and the evolution of the lithosphere, *Earth Planet. Sci. Lett.*, *144*, 93–108, 1996.

Intergovernmental Oceanographic Commission (IOC), GEBCO-97: The 1997 Edition of the GEBCO Digital Atlas, Paris, 1997.

Ito, G., and J. Lin, Oceanic spreading center-hotspot interactions: Constraints from along-isochron bathymetric and gravity anomalies, *Geology*, *7*, 657–660, 1995.

Ito, G., J. Lin, and C. W. Gable, Dynamics of mantle flow and melting at a ridge-centered hotspot: Iceland and the Mid-Atlantic Ridge, *Earth Planet. Sci. Lett.*, *134*, 155–168, 1996.

Ito, G., Y. Shen, G. Hirth, and C. J. Wolfe, Mantle flow, melting, and dehydration of the Iceland mantle plume, *Earth Planet. Sci. Lett.*, *165*, 81–96, 1999.

Lin, J., and J. Phipps Morgan, The spreading rate dependence of three-dimensional mid-ocean ridge gravity structure, *Geophys. Res. Lett.*, *19*, 13–16, 1992.

Macdonald, K. C., Mid-ocean ridges: Fine scale tectonic, volcanic, and hydrothermal processes within the plate boundary zone, *Ann. Rev. Earth Planet. Sci.*, *10*, 155–190, 1982.

Phipps Morgan, J., The generation of a compositional lithosphere by mid-ocean ridge melting and its effect on subsequent off-axis hotspot upwelling and melting, *Earth Planet. Sci. Lett.*, *146*, 213–232, 1997.

Phipps Morgan, J., W. J. Morgan, Y. S. Zhang, and W. H. F. Smith, Observational hints for a plume-fed, suboceanic asthenosphere and its role in mantle convection, *J. Geophys. Res.*, *100*, 12,753–12,767, 1995.

Pollitz, F. F., and I. S. Sacks, Viscosity structure beneath northeast Iceland, *J. Geophys. Res.*, *101*, 17,771–17,793, 1996.

Reid, I., and H. R. Jackson, Oceanic spreading rate and crustal thickness, *Mar. Geophys. Res.*, *5*, 165–172, 1981.

Ribe, N. M., U. R. Christensen, and J. Theissing, The dynamics of plume-ridge interaction: Part 1. Ridge-centered plumes, *Earth Planet. Sci. Lett.*, *134*, 155–168, 1995.

Schilling, J.-G., Fluxes and excess temperatures of mantle plumes inferred from their interaction with migrating mid-ocean ridges, *Nature*, *352*, 397–403, 1991.

Schouten, H., K. D. Klitgord, and J. A. Whitehead, Segmentation of mid-ocean ridges, *Nature*, *317*, 225–229, 1985.

Shen, Y., and D. W. Forsyth, The effects of temperature- and pressure-dependent viscosity on three-dimensional passive flow of the mantle beneath a ridge-transform system, *J. Geophys. Res.*, *97*, 19,717–19,728, 1992.

Sigmundsson, F., and P. Einarsson, Glacio-isostatic crustal movements caused by historical volume changes of the Vatnajokull ice cap, Iceland, *Geophys. Res. Lett.*, *19*, 2123–2126, 1992.

Sleep, N. H., Lateral flow of hot plume material ponded at sublithospheric depths, *J. Geophys. Res.*, *101*, 28,065–28,083, 1996.

Toomey, D. R., W. S. D. Wilcock, J. A. Conder, D. W. Forsyth, J. D. Blundy, E. M. Parmentier, and W. C. Hammond, Asymmetric mantle dynamics in the MELT region of the East Pacific Rise, *Earth Planet. Sci. Lett.*, *200*, 287–295, 2002.

Vogt, P. R., Plumes, subaxial pipe flow, and topography along the mid-oceanic ridge, *Earth Planet. Sci. Lett.*, *29*, 309–325, 1976.

Vogt, P. R., and G. L. Johnson, Transform faults and longitudinal flow below the midoceanic ridge, *J. Geophys. Res.*, *80*, 1399–1428, 1975.

Yale, M. M., and J. Phipps Morgan, Asthenosphere flow model of hotspot-ridge interactions: A comparison of Iceland and Kerguelen, *Earth Planet. Sci. Lett.*, *161*, 45–56, 1998.